AD_____

Award Number: W81XWH-06-1-0726

TITLE: Correlative Feature Analysis for Multimodality Breast CAD

PRINCIPAL INVESTIGATOR: Yading Yuan

CONTRACTING ORGANIZATION: University of Chicago
Chicago, Illinois 60637

REPORT DATE: September 2007

TYPE OF REPORT: Annual

PREPARED FOR: U.S. Army Medical Research and Materiel Command
Fort Detrick, Maryland 21702-5012

DISTRIBUTION STATEMENT: Approved for Public Release;
Distribution Unlimited

REPORT DOCUMENTATION PAGE

Form Approved
OMB No. 0704-0188

1. REPORT DATE *(DD-MM-YYYY)*	**2. REPORT TYPE**	**3. DATES COVERED** *(From - To)*
01-09-2007	Annual	1 SEP 2006 - 31 AUG 2007

4. TITLE AND SUBTITLE

Correlative Feature Analysis for Multimodality Breast CAD

5a. CONTRACT NUMBER

5b. GRANT NUMBER
W81XWH-06-1-0726

5c. PROGRAM ELEMENT NUMBER

6. AUTHOR(S)
Yading Yuan

E-Mail: yading@uchicago.edu

5d. PROJECT NUMBER

5e. TASK NUMBER

5f. WORK UNIT NUMBER

7. PERFORMING ORGANIZATION NAME(S) AND ADDRESS(ES)

University of Chicago
Chicago, Illinois 60637

8. PERFORMING ORGANIZATION REPORT NUMBER

9. SPONSORING / MONITORING AGENCY NAME(S) AND ADDRESS(ES)
U.S. Army Medical Research and Materiel Command
Fort Detrick, Maryland 21702-5012

10. SPONSOR/MONITOR'S ACRONYM(S)

11. SPONSOR/MONITOR'S REPORT NUMBER(S)

12. DISTRIBUTION / AVAILABILITY STATEMENT
Approved for Public Release; Distribution Unlimited

13. SUPPLEMENTARY NOTES

14. ABSTRACT

The purpose of this study is to develop correlative feature analysis methods for integrating image information from multi-modality breast images, taking advantage of the information from different views and/or different modalities, and thus improving the sensitivity and specificity of breast cancer diagnosis. Identifying the corresponding image pair of a lesion is an essential step for this purpose. During the first year, we have collected and maintained a multi-modality breast image database, which includes full-field digital mammography (FFDM), sonography and MRI images. To differentiate corresponding FFDM image pairs from non-corresponding ones, in which images were obtained from CC and ML view respectively, we have developed computerized methods for lesion segmentation, feature extraction and selection, feature correlation analysis and image pair classification. The results have shown that our computerized feature correlative analysis has great potential in identifying the corresponding image pair of a lesion obtained from different views of the same modality.

15. SUBJECT TERMS
Multi-modality database, lesion segmentation, feature extraction, feature selection

16. SECURITY CLASSIFICATION OF:			**17. LIMITATION OF ABSTRACT**	**18. NUMBER OF PAGES**	**19a. NAME OF RESPONSIBLE PERSON**
a. REPORT	**b. ABSTRACT**	**c. THIS PAGE**			USAMRMC
U	U	U	UU	60	**19b. TELEPHONE NUMBER** *(include area code)*

Table of Contents

Page

INTRODUCTION

It has been well recognized that merging information from different imaging modalities, such as mammography, sonography and magnetic resonance imaging (MRI), will greatly benefit the diagnosis of breast cancer [1-4], as well as contribute to the assessment of tumor response and image-guided therapy. However, interpreting images from different modalities is not trivial as different images of the same lesion may exhibit different physical lesion characteristics, and the image acquisitions are performed under different breast positioning protocols. Also, the breast is a non-rigid object, and thus conventional image registration methods are not appropriate. So the primary problem of merging image information from different modalities is to address the task of identifying corresponding images of lesions as seen with different imaging techniques. The purpose of this research is to develop correlative feature analysis methods for integrating image information from multi-modality breast images, taking advantage of the information from different views and/or different modalities, and thus improving the sensitivity and specificity of breast cancer diagnosis. A novel aspect of the proposed research is the development of correlative feature analysis (CFA) into the decision-making process. Our hypothesis is that the proposed correlative feature analysis can benefit computerized corresponding image analysis, thus help the radiologist efficiently distinguish between corresponding and non-corresponding lesion pairs. This report summarizes the progress of this Predoctoral Traineeship Award project made by the recipient during the first year.

BODY

Training Accomplishments

At the time of this report, the recipient, Yading Yuan, of the Predoctoral Traineeship Award has taken 21 out of the 22 required courses towards the Ph.D. degree in medical physics. The remaining one course will be taken in 2007, Fall. The courses include physics of medical imaging, physics of radiation therapy, mathematics for medical physicists, image processing, statistics, machine learning, numerical computation, computer vision, anatomy of the body, radiation biology, and teaching assistant training.

Research Accomplishments

1. Database collection

The first part of our work has been collecting a multi-modality image database from the University of Chicago Hospitals, which includes full-field digital mammographic (FFDM) images, breast ultrasound (US) images and breast magnetic resonance (MR) images. The FFDM database consists of 148 malignant and 139 benign lesions. All the images were obtained from GE Senographe 2000D systems with a spatial resolution of 95μm×95μm. The US database consists of 195 malignant solid lesions, 77 simple cysts, 25 fibrocystic nodules and 109 benign solid lesions. The US images were obtained with a Philips HDI 5000 US unit and a 12-5MHz linear array probe. The pixel size varied from 53 μm to 212 μm, with the average value of 114 μm. The MR database consists of 97 malignant and 84 benign lesions. The MR images were obtained from 1.5T GE scanners using T1-weighted 3D spoiled gradient echo sequences. For each case, one pre-contrast and five post-contrast series were taken and each series contained 60 coronal slices with a range of planar spatial resolution from $1.25\times1.25mm^2$ to $1.6\times1.6mm^2$. Slice thickness ranged from 3 to 4 mm depending on breast size. All the cases in the multi-modality database were identified by expert breast radiologists based on visual criterion and either biopsy or aspiration proven reports.

Based on the FFDM database, we constructed 123 corresponding image pairs and 82 non-corresponding pairs. Each pair consists of a craniocaudal (CC) view and a mediolateral (ML) view. Considering the most realistic scenario of lesion mismatch in clinical practice, the non-corresponding pairs were constructed from cases of the same patients but different physical lesions. Since in our database the number of patients having two or more lesions in the same breast is limited, the non-corresponding dataset included all possible lesion combinations from different views.

With the whole multi-modality database, we also constructed a dataset with 112 cases having both mammography and sonography. By incorporating MR images, there are 88 cases having all the three modality images so far. We are currently having radiologists determine the correspondence of lesions appeared in different modality images.

2. Investigation of lesion segmentation

Mass lesion segmentation on mammograms is a challenging task since mass lesions are usually embedded and hidden in varying densities of parenchymal tissue structures. We have developed a dual-stage method for automatic delineation of lesion boundaries on FFDM images. This method utilizes a geometric active contour model that minimizes an energy function based on the homogeneities inside and outside of the evolving contour. Prior to the application of the active contour model, a radial gradient index (RGI) based segmentation method is applied to yield an initial contour closer to the lesion boundary location in a computationally efficient manner. Based on the initial segmentation, an automatic background estimation method is applied to identify the effective circumstance of lesion, and a dynamic stopping criterion is implemented to terminate the contour evolution when it reaches the lesion boundary. By using the FFDM database described above, we quantitatively compare the proposed algorithm with a conventional region-growing method and a RGI-based algorithm by use of the area overlap ratio between computer segmentation and manual segmentation by an expert radiologist. At an overlap threshold of 0.4, 85% of the images are correctly segmented with the proposed method, while only 69% and 73% of the images are correctly delineated by our previous developed region-growing and RGI method. A full description of the method is in reference [5] which is attached as Appendix A.

3. Investigation of feature correlation

We evaluated the correlation performance of individual computerized features extracted from the FFDM images of a lesion obtained in CC and ML views. In order to evaluate the robustness of the correlation performance to lesion segmentation, besides the radiologist's outlines, three automatic segmentation methods were employed to extract the mass lesion from the surrounding tissues, which includes a conventional region-growing method, a RGI-based method and the newly-developed dual-stage segmentation method. 15 computer-extracted features of each lesion were calculated in both views in order to quantify the characteristics of margin, shape, contrast and texture of the lesion. For each feature, correlation coefficient between the two views and the p-value of the derived correlation coefficient were obtained. Our results show that the features characterizing shape, contrast and texture performed better among the 15 individual features despite of segmentation methods and pathology. This is because the features representing large-scale information are less sensitive to the change of position than those representing small-scale information, which results in the higher correlation between large-scale features from different views than that of small-scale features. This work provides a guide for discriminating corresponding and non-corresponding lesion pairs within the CAD framework. It is also helpful for guiding the development of new features to improve the accuracy of image matching in disease diagnosis and prognosis. A more detailed summary can be found in reference [6], which is also attached as Appendix B.

Mutual information (MI) is another measure of the dependence between two variables. It is well understood that mutual information measures the general dependence, while the correlation coefficient measures the linear dependence. So we also investigated the mutual information among the features and assessed its effect on the choice of

discriminating features as compared with the use of linear correlation coefficient between features. For each feature described above, mutual information between the two views was obtained using a density estimation method (e.g., Parzen windows). However, the dependence rank of features determined by mutual information highly agreed with that determined by linear correlation coefficient, yielding a correlation coefficient of 0.87. This result indicated that linear correlation coefficient is a good metric to represent the dependence between features from different views. Moreover, since linear correlation coefficient is bounded to [-1,1], we will use linear correlation coefficient as the metric to choose the discriminating features.

4. Development of new computerized features

Since features characterizing large-scale information usually have better correlation performance, we developed two sets of "large-scale" features. Firstly, we extracted a set of texture features based on a gray-level co-occurrence matrix (GLCM). For each region, four GLCMs were constructed along four different directions of 0°, 45°, 90° and 135°. Assuming that there is no directional texture features in mammograms, a non-directional GLCM was obtained by summing all the directional GLCMs. Texture features were then computed from each non-directional GLCM. To avoid sparse GLCMs for smaller lesions, the gray level range of image was scaled down to 6 bits, resulting in GLCM of size 64×64. Among the texture features, correlation feature performed best with a correlation coefficient of 0.67 (p-value < 10^{-3}).

In clinic practice, radiologists commonly use the distance from nipple to the center of a lesion to correlate the lesion in different views. It is generally believed that this distance keeps fairly constant. Thus, we developed a distance feature to measure the Euclidean distance between the nipple location and the mass center of lesion. We also developed an automatic nipple localization scheme to tracking nipple markers on each FFDM images. With computer-identified nipples, the distance features in CC views are highly correlated with those in ML views, yielding a correlation coefficient of 0.88 (p-value < 10^{-3}).

5. Evaluation of the performance of computerized features for the task of distinguishing corresponding image pairs and non-corresponding ones

We used the FFDM database to evaluate the performance of computerized features for the task of distinguishing corresponding and non-corresponding image pairs from CC and ML views [7]. 17 features that were automatically extracted from the lesions could be grouped into three categories: (I) density and morphological features; (II) texture features and (III) distance feature. A stepwise feature selection procedure was employed to select an effective subset of features, which were then combined by Bayesian artificial neural networks (BANN) to obtained a discriminant score, yielded an estimate of the probability that the two images are of the same physical lesion. Receiver characteristic (ROC) analysis was used to evaluate the classification performance of the individual features and the selected feature subset. The distance feature yielded an AUC (area under the ROC curve) of 0.81 with leave-one-out cross-validation, and the feature subset with 3 features yielded an AUC of 0.86. The preliminary study, which includes 124 corresponding and

35 non-corresponding image pairs, has been submitted to SPIE Medical Imaging Conference, 2008. The abstract is attached as Appendix C.

KEY RESEARCH ACCOMPLISHMENTS

- Collected and maintained a multi-modality database including full-field digital mammograms, breast ultrasound images and breast MR images. More than 180 lesions were collected for each modality, which is suitable for the further correlative feature analysis across image modalities.

- Developed a dual-stage lesion segmentation method for FFDM images, which outperformed the performances of our previous developed region-growing method and the RGI-based segmentation method.

- Investigated feature correlation with both linear correlation coefficient and mutual information. The results demonstrate that the features representing large-scale information of lesions usually have better correlation performance and linear correlation coefficient is an appropriate metric characterizing the dependence between features from different views.

- Developed texture features and distance feature, which have been proven to be useful in differentiating corresponding and non-corresponding image pairs.

- Evaluated the performance of computerized features for the task of distinguishing corresponding and non-corresponding image pairs. The selected feature subset yielded an AUC of 0.86 with leave-one-out cross-validation.

REPORTABLE OUTCOMES

Peer-reviewed Journal Papers

- Y. Yuan, M. L. Giger, H. Li, K. Suzuki and C. Sennett, "A dual-stage method for lesion segmentation on digital mammograms", Med. Phys, (In press), 2007.

Conference Proceeding Papers

- M. L. Giger, Y. Yuan, H. Li, K. Drukker, W. Chen, L. Lan and K. Horsch, "Progress in breast CADx, " Biomedical imaging: From Nano to Macro, 2007. ISBI 2007. 4th IEEE International Symposium on, Arlington, Virginia, 2007

- H. Li, M. L. Giger, Y. Yuan, L. Lan, K. Suzuki, A. Jamieson and C. Sennett, "Comparison of computerized image analyses for digitized mammograms and FFDM images, " International Workshops on Digital Mammography, Manchester, United Kingdom, 2006

Conference Presentations and Abstracts

- Y. Yuan, M. L. Giger, H. Li and C. Sennett, "Correlative feature analysis of FFDM images", submitted to SPIE Medical Imaging Conference, 2008.

- Y. Yuan, M. L. Giger, H. Li and C. Sennett, "Computer-based feature correlation on multiple-view FFDM images", Radiological Society of North America, Chicago, Illinois, 2006

CONCLUSIONS

The recipient of the Predoctoral Traineeship Award has taken all the required core courses and many research related elective courses as well. These trainings have proven useful for the recipient to achieve the proposed research goals.

During the first year, we have collected and maintained a multi-modality database including full-field digital mammograms, breast ultrasound images and breast MR images, which is suitable for the proposed research on correlative feature analysis for multi-modality images. We have developed computerized methods for lesion segmentation, feature extraction and selection, feature correlation analysis and image pair classification in differentiating corresponding and non-corresponding FFDM image pairs from CC and ML views, respectively. The results have shown that our computerized feature correlative analysis has great potential in identifying the corresponding image pair of a lesion for FFDM images.

Overall, we have achieved the goals for the first year and laid down a good foundation for the research in the next two years. Our goals in the next two years include collection of more image data, development of feature selection method based on mutual information and compare it with stepwise feature selection and genetic algorithm-based feature selection methods, investigation of features that would have better correlation between image pairs across different image modalities, and evaluation of the proposed feature correlative analysis with the whole multi-modality database.

REFERENCES

[1] S. H Heywang-Kobrunner, D. D Dershaw, and I. Schreer, "Diagnostic breast imaging: Mammography, sonography, magnetic resonance imaging, and interventional procedures," Thieme Medical Publishers, 2nd Edition, 2001.

[2] K. Horsch, M. L. Giger, L. A. Venta, and C. J. vyborny, "Computerized diagnosis of breast lesions on ultrasound," Med. Phys., 29, 157-164, 2002.

[3] G. M. Newstead, "Role of MR in breast imaging," RSNA Categorical Course in Breast Imaging, 287-293, 1999.

[4] K. Drukker, K. Horsch and M. L. Giger, "Multimodality computerized diagnosis of breast lesons using mammography and sonography" , Acad. Radiol. 12, 970-979, 2005.

[5] Y. Yuan, M. L. Giger, H. Li, K. Suzuki and C. Sennett, "A dual-stage method for lesion segmentation on digital mammograms", Med. Phys, (In press), 2007.

[6] Y. Yuan, M. L. Giger, H. Li and C. Sennett, "Computer-based feature correlation on multiple-view FFDM images", Radiological Society of North America, Chicago, Illinois, 2006

[7] Y. Yuan, M. L. Giger, H. Li and C. Sennett, "Correlative feature analysis of FFDM images", submitted to SPIE Medical Imaging Conference, 2008.

APPENDICES

- Appendix A: Y. Yuan, M. L. Giger, H. Li, K. Suzuki and C. Sennett, “A dual-stage method for lesion segmentation on digital mammograms”, Med. Phys, (In press), 2007.
- Appendix B: Y. Yuan, M. L. Giger, H. Li and C. Sennett, “Computer-based feature correlation on multiple-view FFDM images”, Radiological Society of North America, Chicago, Illinois, 2006
- Appendix C: Y. Yuan, M. L. Giger, H. Li and C. Sennett, “Correlative feature analysis of FFDM images”, submitted to SPIE Medical Imaging Conference, 2008.

A dual-stage method for lesion segmentation on digital mammograms

September 24, 2007

Yading Yuan, Maryellen L. Giger, Hui Li, Kenji Suzuki and Charlene Sennett

Department of Radiology, Committee on Medical Physics, The University of Chicago

Send Correspondence To:

Yading Yuan

Department of Radiology, The University of Chicago

5841 South Maryland Avenue, MC 2026

Chicago, IL 60637

E-mail: yading@uchicago.edu

Phone: (773) 834-5101

Fax: (773) 702-0371

Abstract

Mass lesion segmentation on mammograms is a challenging task since mass lesions are usually embedded and hidden in varying densities of parenchymal tissue structures. In this paper, we present a method for automatic delineation of lesion boundries on digital mammograms. This method utilizes a geometric active contour model that minimizes an energy function based on the homogeneities inside and outside of the evolving contour. Prior to the application of the active contour model, a radial gradient index (RGI) based segmentation method is applied to yield an initial contour closer to the lesion boundary location in a computationally efficient manner. Based on the initial segmentation, an automatic background estimation method is applied to identify the effective circumstance of lesion, and a dynamic stopping criterion is implemented to terminate the contour evolution when it reaches the lesion boundary. By using a full-field digital mammography database with 739 images, we quantitatively compare the proposed algorithm with a conventional region-growing method and a RGI-based algorithm by use of the area overlap ratio between computer segmentation and manual segmentation by an expert radiologist. At an overlap threshold of 0.4, 85% of the images are correctly segmented with the proposed method, while only 69% and 73% of the images are correctly delineated by our previous developed region-growing and RGI methods, respectively. This resulting improvement in segmentation is statistically significant.

Key words: Mass lesion segmentation, geometric active contour model, computer-aided diagnosis, breast cancer

I. INTRODUCTION

Breast cancer is the most common malignancy in American women and the second most common cause of death from malignancy in this population. According to the American Cancer Society, about 178,480 women in the United States will be found to have invasive breast cancer in 2007, and about 40,460 women will die from the disease this year [1]. Although some imaging modalities, such as magnetic resonance imaging (MRI)[2][3] and sonography[4][5], are currently being investigated to improve sensitivity and specificity of breast cancer diagnosis, X-ray mammography is still the most prevalent imaging procedure for the early detection of breast cancer.

Lesion segmentation, which extracts the lesion from the surrounding tissues, is an essential step in the computerized analysis of mammograms. As mass lesions are usually embedded and hidden in varying densities of parenchymal structures, the task of lesion segmentation is not trivial. Many researchers have developed computer algorithms for this task. Huo et al. [6] employed a region-growing method to find the contour, in which abrupt changes in size and circularity were used as the rules of segmentation. Kupinski et al. [7] segmented the mass by applying either a radial gradient index (RGI) model or a probabilistic model to the lesion, multiplied by a constraint function. Petrick et al. [8] introduced a segmentation algorithm that combines a density-weighted contrast enhancement filter and a region growing method. Li et al. [9] employed a multiresolution Markov random field model to detect tumors in mammographic images. Timp et al. [10] employed both edge based information as well as a priori knowledge about the grey level distribution of the region of interest (ROI) around the mass, and obtained an optimal contour using dynamic programming. To segment lesions, Guliato et al. [11] proposed two fuzzy sets related methods – one employing a region growing after fuzzy-sets-based pre-processing, and the other using a fuzzy region-growing method that takes into account the uncertainty present around the boundaries of tumor. Li et al. [12] presented a statistical model for enhanced segmentation and extraction of a suspicious mass area from mammographic images. In their study, a morphological operation

is derived to enhance disease patterns of suspected masses by eliminating unrelated background clutter, and a model-based image segmentation is performed to localize the suspected mass areas using stochastic relaxation labeling.

Originally introduced by Kass [13], active contour models (or snakes) have attracted much attention as image segmentation techniques. An active contour model minimizes an energy functional along a deformable contour, which is influenced by both internal and external terms. The internal energy controls the smoothness and elasticity of the contour, while the external energy attracts the evolving contour to deform toward salient image features, such as edges. Although the active contour model has been used for segmenting objects in a wide range of medical applications [14][15][16][17][18][19], to the best of our knowledge, few works have applied this model to the task of lesion segmentation in mammographic images. Brake et al. [20], segmented mass lesions by a discrete active contour method whose external energy was determined by the image gradient magnitude. Sahiner et al. [21] applied an active contour model that incorporated edge and region analysis, in which the contour energy was minimized by a greedy algorithm. In their work, however, the contour was represented by the vertices of an N-points polygon and each vertex was tracked during the process, which makes it difficult for the contour to adapt to a change of topology, such as splitting or merging parts.

Differing from the segmentation methods mentioned above, in this study, we develop an automatic lesion segmentation algorithm that employs a geometric active contour model to extract lesions. Geometric active contour models [22][23] represent contours as a level set of a higher-dimensional scalar function[24]. The contours are obtained only after complete evolution, thereby allowing the model to handle the topological changes naturally. As mass lesions usually have weak edges, we use a region-based active contour model [25] that is based on global image information, and is less sensitive to noise and the initial contour. In order to improve the computational efficiency and suppress the influence of unrelated structures, our previous RGI-based segmentation method[7] is applied first to delineate an initial contour,

which is relatively close to the actual margin, and to estimate the effective background. We then exploit a dynamic stopping criterion, which is solely based on the property of the given image, to terminate the evolving procedure automatically.

The organization of this paper is as follows: Section 2 introduces the database used for this study. Section 3 describes the proposed segmentation method. Section 4 presents the results, and Section 5 and 6 give a discussion and conclusion, respectively.

II. MATERIALS

In this study, we used a full-field digital mammography (FFDM) database, which consists of 139 benign (327 mammograms) and 148 malignant (412 mammograms) lesions. All the images were collected from the University of Chicago Hospitals (UCH) and obtained from GE Senographe 2000D systems (GE Medical Systems, Milwaukee, WI) with a spatial resolution of $95\,\mu m \times 95\,\mu m$. The masses were identified and outlined by an expert breast radiologist based on visual criterion and biopsy-proven reports. These outlines were used as the "gold standard" for calibrating parameters and evaluating performace. The distributions of effective projection diameter, which is defined as the effective diameter of the area inside the radiologist's manually-delineated contours, are shown in Fig. 1.

[Figure 1 about here.]

III. METHODS

The main aspects of the proposed segmentation method include an initial RGI segmentation[7], background estimation and trend correction, and an active contour segmentation based on level sets. Fig. 2 shows the flow chart of the overall implementation.

[Figure 2 about here.]

A. Active contour model

The active contour model [25] relies on an intrinsic property of image segmentation: for an image formed by two regions, each segmented region should be as homogeneous as possible. Mathematically, this model can be expressed by the following energy function:

$$\begin{aligned} E(c_1,\, c_2,\, C) \;&=\; \mu \cdot Length(C) \\ &\quad +\lambda_1 \cdot \int_{inside(C)} |f_0(x,\, y) \,-\, c_1|^2 dxdy \\ &\quad +\lambda_2 \cdot \int_{outside(C)} |f_0(x,\, y) \,-\, c_2|^2 dxdy \end{aligned} \tag{1}$$

where $\mu \geq 0,\ \lambda_1,\ \lambda_2 > 0$ are fixed weight parameters, C is the evolving contour and $Length(C)$ is a regularizing term that prevents the final contour from converging to a small area due to noise, and c_1 and c_2 are mean values inside and outside of C, respectively. Note that many other active contour models are edge-based as opposed to the gray-level based method used here.

Equation (1) can be represented and solved by level set theory [26]. Level set theory, in which the two-dimensional evolving contour C is represented implicitly as the zero level set of a three-dimensional Lipschitz function $\phi(x,\, y)$, i.e. $C = \{(x,\, y) \in \Omega :\ \phi(x,\, y) = 0\}$, evolves the contour by updating the level set function $\phi(x,\, y)$ at fixed coordinates through iterations instead of tracking the contour itself. The initial level set function $\phi(x, y)$ is usually defined as the signed distance function:

$$\phi(x,\, y;\, t = 0) = \pm d \tag{2}$$

where d is the distance from $(x,\, y)$ to $C(t = 0)$, where $C(t = 0)$ corresponds to the initial contour. The plus (minus) sign is chosen if the point $(x,\, y)$ is inside (outside) the initial contour $C(t = 0)$.

With the evolution of the contour, the level set function ϕ cannot be held as a signed distance function, nor can it be kept smooth. In order to maintain a smooth level set function, and thus ensure numerical stability of evolution, it is necessary to *reinitialize* the evolving level set function to a signed distance function periodically. However, reinitialization is a computationally consuming procedure as it evolves solving the partial differential equation $\phi_t = sign(\phi_t)(1- \parallel \nabla\phi_t \parallel)$, where $\nabla\phi_t$ corresponds to the gradient of the level set function. In addition, most reinitializing schemes tend to move the contour to some degree due to numerical errors [27].

A signed distance function ϕ, however, has the intrinsic property that $\parallel \nabla\phi \parallel = 1$. Thus, it is more natural to incorporate this property into the contour evolution instead of using the independent reinitializaing procedure described above. Thus, we can introduce another regularizing term [28] in the active contour model in (1) :

$$\begin{aligned} E(c_1,\, c_2,\, C) \;\; = \;\; & \mu \cdot Length(C) \\ & + \nu \cdot \frac{1}{2} \int_{\Omega} (1- \parallel \nabla\phi_t \parallel)^2 dxdy \\ & + \lambda_1 \cdot \int_{inside(C)} |f_0(x,\, y) \,-\, c_1|^2 dxdy \\ & + \lambda_2 \cdot \int_{outside(C)} |f_0(x,\, y) \,-\, c_2|^2 dxdy \end{aligned} \tag{3}$$

where ν is a weighted parameter and Ω represents the whole image space.

By replacing C with $\phi(x,\, y)$ in the energy functional in (3) and introducing the regularized versions of the Heaviside function $H_\epsilon(\phi) = \frac{1}{2}[1 + \frac{2}{\pi} arctan(\frac{\phi}{\epsilon})]$along with the corresponding Dirac measure $\delta_\epsilon(\phi) = \frac{d}{d\phi} H_\epsilon(\phi) = \epsilon \cdot [\pi \cdot (\epsilon^2 + \phi^2)]^{-1}$, as given by Chen and Vese in [25], Equation (3) can be expressed as:

$$
\begin{aligned}
E_\epsilon(c_1, c_2, \phi) &= \mu \cdot \int_\Omega \delta_\epsilon(\phi(x,y)) \parallel \nabla\phi(x,y) \parallel dxdy \\
&\quad +\nu \cdot \frac{1}{2} \int_\Omega (1 - \parallel \nabla\phi(x,y) \parallel)^2 dxdy \\
&\quad +\lambda_1 \cdot \int_\Omega |f_0(x,y) - c_1|^2 H_\epsilon(\phi(x,y)) dxdy \\
&\quad +\lambda_2 \cdot \int_\Omega |f_0(x,y) - c_2|^2 (1 - H_\epsilon(\phi(x,y))) dxdy
\end{aligned} \tag{4}
$$

where the first integral controls the length of the contour and the second integral helps to smooth the level set function and thus avoid the need for reinitialization.

By fixing c_1 and c_2 and minimizing E_ϵ in terms of ϕ at each iteration, the associated Euler-Lagrange equation can be derived as:

$$
\delta_\epsilon(\phi) \cdot [\mu \cdot \kappa - \lambda_1 \cdot (f_0 - c_1)^2 + \lambda_2 \cdot (f_0 - c_2)^2] + \nu \cdot div[(1 - \frac{1}{\parallel \nabla\phi \parallel}) \cdot \nabla\phi] = 0 \tag{5}
$$

where

$$
\kappa = div(\frac{\nabla\phi}{\|\nabla\phi\|}) \tag{6}
$$

represents the curvature of the contour C, and which also now incorporates the regularizing term from Li *et. al.*[28]. This derivation, combining the aspect of active contour without edges and level set without reinitialization, is given in the Appendix I. Using the gradient descent method, we can solve ϕ in Equation (5) iteratively by letting ϕ be a function of iteration t and replace the zero on the right-hand side of (5) by the time derivative of ϕ. Thus, we obtain a partial differential equation as:

$$
\frac{\partial\phi}{\partial t} = \delta_\epsilon(\phi) \cdot [\mu \cdot \kappa - \lambda_1 \cdot (f_0 - c_1)^2 + \lambda_2 \cdot (f_0 - c_2)^2] + v \cdot div[(1 - \frac{1}{\parallel \nabla\phi \parallel}) \cdot \nabla\phi]. \tag{7}
$$

The time derivative $\frac{\partial\phi}{\partial t}$was approximated by a forward finite difference:

$$\frac{\delta\phi}{\delta t} = \frac{\phi^{n+1} - \phi^n}{\Delta t} \tag{8}$$

while considering the numerical stability of the PDE solution, the curvature κ was approximated by a discretizing scheme that combines both foward and backward finite differences, as suggested in [29].

$$\begin{aligned} \kappa &= \Delta_-^x \left(\frac{\Delta_+^x \phi_{i,j}^n}{((\Delta_+^x \phi_{i,j}^n)^2 + (m(\Delta_+^y \phi_{i,j}^n,\, \Delta_-^y \phi_{i,j}^n)^2)^{1/2}} \right) \\ &\quad + \Delta_-^y \left(\frac{\Delta_+^y \phi_{i,j}^n}{((\Delta_+^y \phi_{i,j}^n)^2 + (m(\Delta_+^x \phi_{i,j}^n,\, \Delta_-^x \phi_{i,j}^n)^2)^{1/2}} \right) \end{aligned} \tag{9}$$

where

$$\Delta_\mp^x = \mp(\phi_{i\mp1,j} - \phi_{i,j}) \tag{10}$$

and similarly for $\Delta_\mp^y \phi_{i,j}$.

$$m(a,\, b) = \left(\frac{sng(a) + sng(b)}{2} \right) min(|a|,\, |b|). \tag{11}$$

B. Contour initialization

The energy function in Equation (3) depends on the evolving curve C in a complex way. It is not guaranted to be quadratic or even convex, and one might find a local minimum of the energy function somewhere in the neighborhood of the initial contour. Thus, initializing the contour is a non-trivial task for active contour models. Since lesions' sizes vary, it is difficult to find fixed parameters (such as the radius of a circle) with which to initialize the contour for an entire database. Hence, we use our previous RGI-based segmentation method[7] to estimate the initial boundary of a lesion.

The RGI-based segmentation algorithm[7] incorporates prior knowledge that mass le-

sions are roughly compact, and thus, the original image $f(x, y)$ is multiplied with a two-dimensional constraint function $G(x, y; \mu_x, \mu_y, \sigma^2)$ to yield a pre-processed image $h(x, y)$ as:

$$h(x, y) = f(x, y) \times G(x, y; \mu_x, \mu_y, \sigma^2) \tag{12}$$

where $G(x, y; \mu_x, \mu_y, \sigma^2)$is a Gaussian function centered at the manually-indicated seed point (μ_x, μ_y), and with variance σ^2. The multiplication with the Gaussian function reduces the contribution of structures beyond the lesion, and thus, σ is set to $15mm$ to accommodate most mammographic lesion sizes. We have found that the segmentation performance is not strongly dependent on the choice of σ. Larger lesions can also be segmented even though the small deviations around the margin of the lesion are usually not delineated well.

Starting from the given seed point (μ_x, μ_y), a series of grey level thresholds are then applied to the pre-processed image $h(x, y)$ to yield multiple contours. For each contour, an RGI value is calculated, where RGI is defined as:

$$RGI(\mu_x, \mu_y, C_i) = \frac{\sum\limits_{(x,y)\in C_i} (\nabla h(x, y) \cdot \frac{\hat{r}(x,y)}{\|\hat{r}(x,y)\|})}{\sum\limits_{(x,y)\in C_i} \| \nabla h(x, y) \|} \tag{13}$$

where C_i is the set of points on the ith contour, $\nabla h(x, y)$ is the gradient vector of $h(x, y)$ at point (x, y), $\hat{r}(x, y)/ \| \hat{r}(x, y) \|$ is the normalized radial vector, the direction of which is calculated at position (x, y) with respect to the seed point (μ_x, μ_y). Of these contours, the one yielding the maximum RGI value is chosen as the contour that best delineates the lesion in the initial step.

RGI represents the average proportion of the gradients in the radially outward direction. The strategy of choosing maximum RGI works well for benign lesions as most have circular-like shapes and smooth margins. However, for malignant lesions, because of irregular shapes and spiculate margins, the resulting contours are usually under-grown. Nevertheless, RGI provides a good initial contour for the following evolution driven by active contour model.

C. Background estimation

In the active contour model, contour evolution relies on the competition between the region inside the contour (foreground) and that outside the contour (background). The presence of structure noises such as lymph nodes, parenchyma, and localization markers complicates the background in mammgrams. RGI segmentation provides not only the initial contour, but also a means to estimate the effective background surrounding the lesion. In our study, the effective background is defined as the set of pixels within a given distance d (pixels) from the circumscribed rectangle of the initial contour, as shown in Fig. 3.

[Figure 3 about here.]

Distance d plays an important role in determining the effective background. On one hand, a large d yields a large region and thus better statistics on the background. On the other hand, a small d would not be contaminated by nearby structures. In this study, an automatic scheme was developed to determine the best distance d from a series of candidates.

For a series of distances d_i, $i = 1, ..., L$, two series of regions can be determined, as Fig. 4 (a) shows. One series of regions are background candidates B_i (Fig. 4 (b)), and the other series are net increases of background B_{Ni} (Fig. 4 (c)), where $B_{Ni} = B_{i+1} - B_i,\ i = 1, ..., L-1$. Our method is based on the following two principles: With the expansion of background, 1) the mean gray value of B_i, i.e. $mean(B_i)$, should decrease as more areas with lower gray level are included; and 2) the standard deviation of B_{Ni} , i.e. $std(B_{Ni})$, should not change substantially for relatively smooth background. By monitoring $mean(B_i)$ and $std(B_{Ni})$ with increasing d_i , two potential distance candidates are obtained. One candidate is defined as the distance at which $mean(B_i)$ reaches a minimum value, and the other candidate is defined as the distance at which $std(B_{Ni})$ demonstrates the maximum increase, as shown in Fig. 5. At last, the final distance is chosen as the minimum of these two candidates. As for the example in Fig. 4, the distance is automatically determined $d = 110$ (pixels).

[Figure 4 about here.]

[Figure 5 about here.]

D. Background trend correction

Due to the non-uniformity of the background distribution, some pixels in the background have similar gray values as in the lesion, which hinders the segmentation performance of the active contour model. Thus, a two-dimensional background trend correction was employed prior to segmentation. The background trend is estimated by fitting a two-dimensional surface with a least-squares method to the gradual change in the background pixel values within the extracted background estimation region. Here, we used a first-order ploynomial function, i.e. $f(x, y) = a+b\cdot x+c\cdot y$, to describe the two-dimensional surface as higher order polynomial functions will estimate mass lesion instead. Fig. 6 demonstrates the significance of the background trend correction when a non-uniform background is present.

[Figure 6 about here.]

E. Dynamic stopping criterion

To stop the evolution of a contour, a pre-determined threshold is often used. Various metrics can be used to check convergence of evolution, such as the change of level set function ϕ [30] and the change of length of contour [31]. The contour evolution can also be terminated when the area inside the contour differs from the initial one by a given value [32]. In our initial study, we had ever defined a stopping criterion of relative foreground change (RFC), which is the ratio between the change of foreground and the area of foreground. Comparing with the stopping criterion of change of contour length used in [31], RFC has two advantages: 1) RFC is a relative measure and thus is more suitable for lesions with various sizes; 2) RFC is more computationally efficient as the aquisition of contour in [31] brings additional computation. No matter the strategy is used, it is necessary to set some threshold in advance. However, due to varying sizes of lesions as well as sizes of background obtained from automatic background

estimation, it is difficult to find a fixed parameter for controlling convergence.

In our preliminary work [33], we developed a dynamic method to terminate contour evolution automatically. In that work, as the contour evolves, mean values of both foreground and background will decrease gradually. As foreground is generally more homogeneous than the background, the rate of foreground mean change is less than that of background mean change. However, as the evolving contour crosses the lesion margin, the foreground mean will decrease faster than will the background mean. Thus, during dynamic contouring, the difference between the rate of foreground mean change and that of background mean change is tracked, and contour evolution is terminated when the decrease of foreground mean value is more rapid than that of the background mean value. This method provides a way to terminate contour evolution free of pre-defined threshold. However, it neglects the influence of sizes of both foreground and background, and thus ceases contour evolution earlier than expected.

In order to address this problem, we modified the previous method, which we present here in one dimension. As Fig. 7 shows, $g(x)$ is a decreasing function defined on the interval [0, L], and point s is moving within [0, L] at the speed of $\vec{v}$. s also splits [0, L] into two regions. For simplicity, the region [0, s] is named region 1, and [s, L] is region 2. Then, the mean values of region 1 and 2 are:

[Figure 7 about here.]

$$c_1 = \frac{\int_0^s g(x)dx}{s}, \qquad c_2 = \frac{\int_s^L g(x)dx}{L-s}.$$

.The slope of c_1 is:

$$\begin{aligned}\frac{dc_1}{dt} &= \frac{dc_1}{ds}\cdot\frac{ds}{dt} \\ &= \frac{d}{ds}(\frac{\int_0^s g(x)dx}{s})\cdot\vec{v} \\ &= \frac{g(s)-c_1}{s}\cdot\vec{v}.\end{aligned}$$

Here, we use the fact that $\vec{v} = \frac{ds}{dt}\cdot\hat{v}$, where $\hat{v}$ is the outward unit vector. Similarly, the slope of c_2 is :

$$\frac{dc_2}{dt} = -\frac{g(s)-c_2}{L-s}\cdot\vec{v}.$$

Thus, the difference between these two slopes is:

$$\Delta v = \frac{dc_1}{dt} - \frac{dc_2}{dt} = (\frac{g(s)-c_1}{s} + \frac{g(s)-c_2}{L-s})\cdot\vec{v}. \tag{14}$$

As the discussed above, as s moves within the object, we have $\Delta v > 0$. As s moves across the edge, Δv will become negative. When $\Delta v = 0$, we have $g(s) = \frac{s}{L}\cdot c_2 + \frac{L-s}{L}\cdot c_1 > \frac{1}{2}(c_1+c_2)$ as in general $L-s > s$ and $c_1 > c_2$. However, if only the speed terms driven by image property in Equation (7) are considered, the evolution should stop at s_0 such that $g(s_0) = \frac{1}{2}(c_1+c_2)$. Because of the influence of sizes, s will stop moving quickly if the criterion in Equation (14) is used.

In order to eliminate the influence of size, a weighted difference between slope of c_1 and that of c_2 is introduced as :

$$\Delta v_w = \frac{s}{L-s}\cdot\frac{dc_1}{dt} - \frac{dc_2}{dt} = \frac{1}{L-s}\cdot[2\cdot g(s) - (c_1+c_2)]\cdot\vec{v}. \tag{15}$$

It can be shown that Δv_w goes to zero at the desired contour s_0, where $g(s_0) = \frac{1}{2}(c_1+c_2)$.

The one-dimensional case, described above, can be extended to two-dimensional one. During the contour evolution, the weighted difference between the mean slope of foreground

and that of backgournd is monitored, and the contour evolution is terminated when the weighted slope difference converges to zero.

F. Implementation

In order to calibrate parameters in the proposed segmentation method, ten digitized screen-film mammograms (SFM) with spatial resolution of $100\mu m \times 100\mu m$ were analyzed. The calibrated segmentation method was then applied to the entire FFDM database for independent performance evaluation.

In our study, we kept both λ_1 and λ_2 in Equation (7) to one (i.e. $\lambda_1 = \lambda_2 = 1$) since the contribution of the homogeneities of inside and outside the contour should be equally considered. Other parameters in Equation (7) were chosen as follows: $\epsilon = 1$ and $\Delta t = 0.1$, where ϵ influences the Heavyside function and Δt controls how quickly the level set function changes. Note that μ controls the smoothness of the final contour. However, If one wants to depict the fine details of the object, one should choose a small μ. On the contrary, if one wants to obtain a smoother contour, one should set a large μ. As some of our computer-extracted features, such as spiculation, characterize the fine details of the lesion margin, we chose a fairly small value of μ, i.e. 0.001×1023^2, which also allows for the use of the 10 bit data. To ensure numerical stability, the coefficient ν must satisfy $\nu \cdot \Delta t < \frac{1}{4}$ [28], so we set $\nu = 2$ in our study. The maximum number of iterations is set to 500.

G. Performance evaluation

The performance of the proposed segmentation algorithm was assessed by comparing the computer-delineated contours with the outlines drawn by an expert breast radiologist. Besides visually evaluating the agreement of computer-segmented results with radiologist's manually-contoured lesion margins, a quantitative measure was used to evaluate the segmentation performance. For a particular lesion, the area overlap ratio (AOR) between manual segmentation and computer segmentation is defined as:

$$AOR = \frac{Area(M \cap C)}{Area(M \cup C)} \tag{16}$$

where M is the manually-segmented contour and C is the computer-segmented contour. AOR ranges from zero to one, being zero in the case of no overlap and one in the case of a perfect match. For the entire database, a series of AOR thresholds were obtained and at each AOR threshold, the percentage of lesions "correctly" segmented was calculated by counting the number of lesions with AOR greater than that threshold.

IV. RESULTS

A. Evaluation of level set smoothness

In our study, a new term $E_S \equiv \int_\Omega (1 - \parallel \nabla \phi_t \parallel) dxdy$ is added to the original active contour model in [25], thus we initially evaluate the usefulness of this term. Two sets of final contours were extracted from the entire FFDM database, one was obtained with E_S and the other without. The results show that E_S can not only provide a smoother contour, but also push the contour closer to the lesion margin with less iterations, yielding a mean number of iterations 160 compared to the mean numer of iterations 327 without E_S. In the example shown in Fig. 8, the left figure shows the segmentation result without smoothing level set function, which took 500 iterations. While for the result with smoothing level set function in the right figure, it only took 248 iterations to converge.

[Figure 8 about here.]

B. Evaluation of dynamic stopping criterion

We investigated our new stopping criterion based on the weighted slope difference between foreground mean and background mean (Δv_w), and compared it to the unweighted slope difference method as well as the relative foreground change (RFC). The RFC thresholds to

terminate contour evolution were set as 0.05, and 0.01, respectively. During the evolution, we recorded the contours using these four stopping criteria and obtained AOR with radiologist's outlines.

Fig. 9 shows plots of the fraction of correctly segmented lesions at various AOR threshold for the four stopping criteria (Δv_w, Δv, $RFC_{0.05}$ and $RFC_{0.01}$) on the FFDM databases. For benign images, all the criteria yielded similar segmentation performances since the initial contours, obtained by RGI segmentation, are close to the true lesion margins. However, as RGI segmentation is inferior for malignant lesions, Δv_w does perform better among all the stopping criteria.

[Figure 9 about here.]

Table 1 summerizes the statistical comparison (Holm t test)[34] among these four criteria, given the mean and standard deviation of AOR for each criterion. In terms of area overlap ratio (AOR), the weighted slope difference method is statistically better than the unweighted slope difference method, and the convergence rate at $RFC = 0.05$ (overall significant level $\alpha^T = 0.05$). However, we failed to show a statistically significant difference between the weighted slope difference method and the convergence rate at $RFC = 0.01$. Nevertheless, if the number of iterations is taken into account, the mean number of iterations for weighted slope difference is 156, while it is 280 for $RFC_{0.01}$. The weighted slope difference is more efficient than $RFC_{0.01}$.

[Table 1 about here.]

C. Comparative evaluation of the segmentation method

The segmentation algorithm was compared with our previously-reported region-growing[6] and RGI-based segmentation[7] methods. Fig. 10 shows several examples of lesion segmentations using these three segmentation methods. The result of the proposed method visually demonstrates a better agreement with the radiologist's outline of the lesion.

[Figure 10 about here.]

Fig. 11 shows the fraction of lesions correctly segmented at various overlap threshold levels. At the overlap threshold of 0.4, for benign lesions, 87% of the images are correctly segmented with the proposed method, while 72% and 81% of the images are correctly segmented by the region-growing and RGI-based methods, respectively. For malignant lesions, 84% of the images are correctly segmented with the proposed method, while 66% and 67% of the images are correctly segmented by region-growing and RGI-based methods, respectively.

[Figure 11 about here.]

Table 2 gives the statistical comparison (Holm t test)[34] for AOR means from the three segmentation methods. The improvement of AOR with the proposed method was found to be statistically significant (overall significant level $\alpha^T = 0.05$).

[Table 2 about here.]

V. DISCUSSION

We developed a dual-stage segmentation method to efficiently segment mass lesions from the parenchymal surround in FFDM images. Our proposed method includes a geometric active contour model, which includes analysis of homogeneities both inside and outside of the evolving contour. The application of RGI-based segmentation to provide initial contour not only improves the computational efficiency, but also provides a method with which to estimate the effective background about the lesion and to suppress unrelated pixel values. Also, our automatic stopping criterion is lesion-specific, and does not rely on fixed iterations.

As the results show, the term E_S in the active contour model plays an important role for effective and efficient segmentation. As $\| \nabla\phi \| > 1$, $div[(1-\frac{1}{\|\nabla\phi\|})\nabla\phi]$ will evolve the level set function ϕ towards reducing $\| \nabla\phi \|$, thus to smooth ϕ. The larger the gradient magnitude of level set function, the more it will be smoothed. While as $\| \nabla\phi \| < 1$, $div[(1-\frac{1}{\|\nabla\phi\|})\nabla\phi]$

will evolve the level set function towards increasing $\| \nabla\phi \|$ to maintain the gradient of the level set function to some level. This mechanism ensures the level set function, and thus the final contour, to be relatively smooth. Meanwhile, as $\| \nabla\phi \|$ is restricted in magnitude, the foreground has the potential to grow faster.

It should be noticed that the weighted slope difference Δv_w is always non-negative as long as $g(x)$ is a decreasing function. In the active contour model, if only the speed term driven by image property is considered, the speed of contour can be simplified as:

$$\begin{aligned} \vec{v} &= [(g(s) - c_2)^2 - (g(s) - c_1)^2] \cdot \hat{v} \\ &= (c_1 - c_2) \cdot [2 \cdot g(s) - (c_1 + c_2)] \cdot \hat{v} \end{aligned}$$

where $\hat{v}$ is the outward unit vector. Inserting $\vec{v}$ into Equation (15), we have:

$$\Delta v_w = \frac{1}{L - s} \cdot (c_1 - c_2) \cdot [2 \cdot g(s) - (c_1 + c_2)]^2 \cdot \hat{v} \geq 0.$$

If $\vec{v}$ is driven by other image property, such as edge information, this relationship still holds. When $g(s) > \frac{1}{2}(c_1 + c_2)$, i.e. s is within the object, the contour will move outward to the edge, thus, we have $\Delta v_w \geq 0$. While if $g(s) < \frac{1}{2}(c_1 + c_2)$, i.e. s is out of object, it will move inward to the edge, we will also have $\Delta v_w \geq 0$. So the weighted slope difference also provides a general mechanism for terminating contour evolution with other active contour models.

In this study, we empirically compared the segmentation performance of the proposed method with our previously-reported region growing[6] and RGI-based[7] segmentation methods. However, it is impossible for us to perform empirical comparisons between our method and those reviewed in the introduction section, as we do not have codes of those methods. Timp's method[10] uses polar coordinate and restricts the mass sizes within certain range, thus one would expect their method to work better for lesions with circular-like margins. However, for lesions with irregular shapes or very large sizes, their method may have dif-

ficulty. Our dual stage segmentation method is able to handle this situation by further evolving the contour via the active contour model. For the fuzzy-set-based methods developed by Guliato et al. [11], both of them need to preset some thresholds such as the gray-level threshold in the first method and the maximum allowed difference between the value of the pixel being analyzed and the mean of the sub-region in the second method, which prevents these methods from being applied in a large database. Their two thresholds were manually selected case by case in their evaluation using a database with 47 mammograms. On the other hand, our method is flexible in that no threshold need to be set in advance.

In our preliminary study [35], we compared two radiologists' outlines with a digitized screen-film mammograms (SFM) database, which consisted of 29 benign (51 mammograms) and 55 malignant (96 mammograms) lesions. At an overlap threshold of 0.4, 96.6% of lesion images were correctly segmented by one radiologist in comparison with the other. This result indicates that the radiologists highly agreed on the lesion margins for SFM. We could expect that the radiologists would also agree on the lesion margins for FFDM as the manufacturer has pre-processed the FFDM images to make them appear to radiologist as traditional-looking SFM mammographs.

When we developed the proposed segmentation algorithm, the FFDM database was being constructed, so our method was initially calibrated and tested with the SFM database [33]. After building the FFDM database, we randomly picked three groups of FFDM images, each of which consisted of five benign and five malignant images, and evaluated the segmentation performance using the proposed method calibrated with SFM images. The results were similar with what we had obtained with SFM images. Thus, we believe that the parameters obtained by SFM also work with FFDM images, which was subsequently validated by the independent evaluation with the entire FFDM database.

Our results could be partially explained by the pre-processing of FFDM images, which is performed by the manufacturers. After pre-processing, the gray-level range and constrast of FFDM images become similar to those of SFM images, which ensures the possibility of

applying parameters from SFM images to FFDM images as gray-level range and contrast are two key components used in our proposed lesion segmentation method. Our results also show the robustness of the proposed method as it mainly uses the global information of images.

VI. CONCLUSION

In this paper, we present a new lesion segmentation method based on a geometric active contour model, which includes an initial RGI segmentation, background estimation, background trend correction, and a dynamic stopping criterion. Evaluation with a large number of FFDM images has shown that the proposed method is statistically superior to our previous region-growing and RGI-based algorithms in terms of overlap ratios obtained in comparison with expert's manual outlines. At an overlap threshold of 0.4, 85% of the images are correctly segmented by the proposed method, while only 69% and 73% of the images are correctly segmented by our previous region-growing and RGI-based methods, respectively.

ACKNOWLEDGMENT

This work was supported in part by US Army Breast Cancer Research Program (BCRP) Predoctoral Traineeship Award (W81XWH-06-1–726), by United States Public Health Service (USPHS) Grant CA89452, and by a grant from the US Army Medical Research and Materiel Command grant (DAMD 98-1209), and by Cancer Center Support Grant (5-P30CA14599). M. L. Giger is a shareholder in R2 Technology, Inc (Sunnyvale, CA), a Hologic Company. It is the University of Chicago Conflict of Interest Policy that investigators disclose publicly actually or potential significant financial interest with would reasonably appear to be directly and significantly affected by the research activities.

APPENDIX

In this part, we provide the details of the derivation from energy function (4) to the associated Euler-Lagrange equation (5). For convenience, we restate Equation (4) here as:

$$\begin{aligned} E_\epsilon(c_1, c_2, \phi) &= \int_\Omega [\mu \cdot \delta_\epsilon(\phi(x,y)) \parallel \nabla\phi(x,y) \parallel \\ &\quad + \frac{v}{2} \cdot (1 - \parallel \nabla\phi(x,y) \parallel)^2 \\ &\quad + \lambda_1 \cdot |f_0(x,y) - c_1|^2 H_\epsilon(\phi(x,y)) \\ &\quad + \lambda_2 \cdot |f_0(x,y) - c_2|^2 (1 - H_\epsilon(\phi(x,y)))] dxdy. \end{aligned} \tag{17}$$

We define $F(\phi, \nabla\phi, x, y)$ as:

$$\begin{aligned} F(\phi, \nabla\phi, x, y) &= \mu\delta_\epsilon(\phi) \parallel \nabla\phi \parallel + \frac{v}{2}(1 - \parallel \nabla\phi \parallel)^2 \\ &\quad + \lambda_1 |f_0 - c_1|^2 H_\epsilon(\phi) + \lambda_2 |f_0 - c_2|^2 (1 - H_\epsilon(\phi)). \end{aligned} \tag{18}$$

For simplicity, we have omitted the independent variables (x, y) of ϕ and f_0. According to Calculus of Variations, the scalar function $\phi(x, y)$ that minimizes $E_\epsilon(c_1, c_2, \phi)$ solves the PDE:

$$\frac{d}{dx}\left(\frac{\partial F}{\partial \phi_x}\right) + \frac{d}{dy}\left(\frac{\partial F}{\partial \phi_y}\right) - \frac{\partial F}{\partial \phi} = 0. \tag{19}$$

Taking the partial derivative of F with respect to ϕ_x, ϕ_y and ϕ, respectively, we have:

$$\frac{\partial F}{\partial \phi_x} = \mu\delta_\epsilon(\phi)\frac{\phi_x}{\parallel \nabla\phi \parallel} + v\left(\phi_x - \frac{\phi_x}{\parallel \nabla\phi \parallel}\right)$$

$$\frac{\partial F}{\partial \phi_y} = \mu\delta_\epsilon(\phi)\frac{\phi_y}{\parallel \nabla\phi \parallel} + v\left(\phi_y - \frac{\phi_y}{\parallel \nabla\phi \parallel}\right)$$

$$\frac{\partial F}{\partial \phi} = \mu \parallel \nabla\phi \parallel \delta_\epsilon^{'}(\phi) + [\lambda_1(f_0 - c_1)^2 - \lambda_2(f_0 - c_2)^2]\delta_\epsilon(\phi) \tag{20}$$

where $\delta_\epsilon^{'} = \frac{d\delta}{d\phi}$ and we use the relation $\parallel \nabla\phi \parallel = \sqrt{\phi_x^2 + \phi_y^2}$.

The partial derivative of $\frac{\partial F}{\partial \phi_x}$ with respective to x is:

$$\frac{d}{dx}(\frac{\partial F}{\partial \phi_x}) = \mu\delta_\epsilon^{'}(\phi)\frac{\phi_x^2}{\parallel \nabla\phi \parallel} + \mu\delta_\epsilon(\phi)\frac{d}{dx}(\frac{\phi_x}{\parallel \nabla\phi \parallel}) + v\frac{d}{dx}[\phi_x - \frac{\phi_x}{\parallel \nabla\phi \parallel}]. \tag{21}$$

Similarly, we have:

$$\frac{d}{dy}(\frac{\partial F}{\partial \phi_y}) = \mu\delta_\epsilon^{'}(\phi)\frac{\phi_y^2}{\parallel \nabla\phi \parallel} + \mu\delta_\epsilon(\phi)\frac{d}{dy}(\frac{\phi_y}{\parallel \nabla\phi \parallel}) + v\frac{d}{dy}[\phi_y - \frac{\phi_y}{\parallel \nabla\phi \parallel}]. \tag{22}$$

Inserting (20) - (22) back to (19), we obtain:

$$\begin{aligned} 0 \;=\; & \mu\delta_\epsilon^{'}(\phi)[\frac{\phi_x^2}{\parallel \nabla\phi \parallel} + \frac{\phi_y^2}{\parallel \nabla\phi \parallel} - \parallel \nabla\phi \parallel] \\ & + \mu\delta_\epsilon(\phi)[\frac{d}{dx}(\frac{\phi_x}{\parallel \nabla\phi \parallel}) + \frac{d}{dy}(\frac{\phi_y}{\parallel \nabla\phi \parallel})] \\ & + v\{\frac{d}{dx}[\phi_x - \frac{\phi_x}{\parallel \nabla\phi \parallel}] + \frac{d}{dy}[\phi_y - \frac{\phi_y}{\parallel \nabla\phi \parallel}]\} \\ & - \delta_\epsilon(\phi)[\lambda_1(f_0 - c_1)^2 - \lambda_2(f_0 - c_2)^2]. \end{aligned} \tag{23}$$

By noticing that:

$$\frac{\phi_x^2}{\parallel \nabla\phi \parallel} + \frac{\phi_y^2}{\parallel \nabla\phi \parallel} = \parallel \nabla\phi \parallel$$

$$\frac{d}{dx}(\frac{\phi_x}{\parallel \nabla\phi \parallel}) + \frac{d}{dy}(\frac{\phi_y}{\parallel \nabla\phi \parallel}) = div(\frac{\nabla\phi}{\parallel \nabla\phi \parallel})$$

and

$$\frac{d}{dx}[\phi_x - \frac{\phi_x}{\parallel \nabla\phi \parallel}] + \frac{d}{dy}[\phi_y - \frac{\phi_y}{\parallel \nabla\phi \parallel}] = div[(1 - \frac{1}{\parallel \nabla\phi \parallel})\nabla\phi]$$

we finally obtain the compact form of (23) as:

$$0 = \delta_\epsilon(\phi)[\mu \cdot div(\frac{\nabla\phi}{\parallel \nabla\phi \parallel}) - \lambda_1(f_0 - c_1)^2 + \lambda_2(f_0 - c_2)^2] + v \cdot div[(1 - \frac{1}{\parallel \nabla\phi \parallel})\nabla\phi]. \quad (24)$$

References

1. A. J. Jemal, R. Siegel, E. Ward, T. Murray, J. Xu, and M. J. Thun. "Cancer statistics, 2007." CA Cancer J. Clin. **57**, 43–66 (2007)

2. G. M. Newstead. "Role of MR in breast imaging." In *RSNA Categorical Course in Breast Imaging* (Chicago, 1999), pp. 287–293

3. S. G. Orel and M. D. Schnall. "MR imaging of the breast for the detection, diagnosis,and staging of breast cancer." Radiology **220**, 13–30 (2001)

4. A. T. Stavros, D. Thickman, C. L. Rapp, M. A. Dennis, S. H. Parker, and G. A. Sisney. "Solid breast nodules: Use of sonography to distinguish between benign and malignant lesions." Radiology **196**, 123–134 (1995)

5. K. Horsch, M. L. Giger, L. A. Venta, and C. J. Vyborny. "Computerized diagnosis of breast lesions on ultrasound." Med. Phys. **29**, 157–164 (2002)

6. Z. Huo, M. L. Giger, C. J. Vyborny, U. Bick, and P. Lu. "Analysis of spiculation in the computerized classification of mammographic masses." Med. Phys. **22**, 1569–1579 (1995)

7. M. A. Kupinski and M. L. Giger. "Automated seeded lesion segmentation on digital mammograms." IEEE Trans. Med. Imaging **17**, 510–517 (1998)

8. N. Petrick, H. P. Chan, B. Sahiner, and M. A. Helvie. "Combined adaptive enhancement and region-growing segmentation of breast masses on digitized mammograms." Med. Phys. **26**, 1642–1654 (1999)

9. H. D. Li, M. Kallergi, L. P. Clarke, and V. K. Jain. "Markov random field for tumor detection in digital mammography." IEEE Trans. Med. Imaging **14**, 565–576 (1995)

10. S. Timp and N. Karssemeijer. "A new 2D segmentation method based on dynamic programming applied to computer aided detection in mammography." Med. Phys. **31**, 958–971 (2004)

11. D. Guliato, R. M. Rangayyan, W. A. Carnielli, J. A. Zuffo, and J. E. L. Desautels. "Segmentation of breast tumors in mammograms using fuzzy sets." J. Electron. Imaging **12**, 369–378 (2003)

12. H. Li, Y. Wang, K. J. R. Liu, S. B. Lo, and M. T. Freedman. "Computerized radiographic mass detection - Part 1: Lesion site selection by morphological enhancement and contextual segmentation." IEEE Trans. Med. Imaging **20**, 289–301 (2001)

13. M. Kass, A. Witkin, and D. Terzopoulos. "Snakes: Active contour models." Int. J. Comput. Vis. **1**, 321–331 (1987)

14. T. Cootes, A. Hill, C. Taylor, and J. Haslam. "The use of active shape models for locating structures in medical images." Image Vis. Comput. **12**, 355–366 (1994)

15. M. S. Atkins and B. Mackiewich. "Fully automatic segmentation of the brain in MRI." IEEE Trans. Med. Imaging **17**, 98–107 (1998)

16. A. Yezzi, S. Kichenassamy, A. Kumar, P. Olver, and A. Tannenbaum. "A geometric snake model for segmentation of medical imagery." IEEE Trans. Med. Imaging **16**, 199–209 (1997)

17. C. Xu, D. L. Pham, and J. L. Prince. "Medical image segmentation using deformable models." In *Handbook of Medical Imaging: Medical Imaging Processing and Analysis*, edited by M. Sonka and M. J. Fitzpatrick (2000), vol. 2 of *Proc. SPIE*, pp. 129–174

18. J. Yang, L. H. Staib, and J. S. Duncan. "Neighbor-constrained segmentation with level set based 3D deformable models." IEEE Trans. Med. Imaging **23**, 940–948 (2004)

19. F. Liu, B. Zhao, and P. K. Kijewski. "Liver segmentation for CT images using GVF snake." Med. Phys. **32**, 3699–3706 (2005)

20. G. M. Brake and N. Karssemeijer. "Segmentation of suspicious densities in digital mammograms." Med. Phys. **28**, 259–266 (2001)

21. B. Sahiner, N. Petrick, H. P. Chan, L. M. Hadjiiski, C. Paramagul, M. A. Helvie, and M. N. Gurcan. "Computer-aided characterization of mammographic masses: accuracy of mass segmentation and its effects on classification." IEEE Trans. Med. Imaging **20**, 1275–1284 (2001)

22. V. Caselles, R. Kimmel, and G. Sapiro. "Geodesic active contours." Int. J. Comput. Vision **22**, 61–79 (1997)

23. R. Malladi, J. A. Sethian, and B. C. Vemuri. "Shape modeling with front propagation: A level set approach." IEEE Trans. Pattern Anal. Machine Intell. **17**, 158–175 (1995)

24. S. Osher and J. A. Sethian. "Fronts propagating with curvature-dependent speed: Algorithms based on Hamilton-Jacobi formulation." J. Comput. Phys. **79**, 12–49 (1988)

25. T. F. Chan and L. A. Vese. "Active contours without edges." IEEE Trans. Image Processing **10**, 266–277 (2001)

26. J. A. Sethian. *Level set methods and fast marching methods: Evolving interfaces in computational geometry, fluid mechanics, computer vision, and materials science* (Cambridge University Press, Cambridge, 1999)

27. S. J. Osher and R. P. Fedkiw. *Level set methods and dynamic implicit surfaces* (Springer, 2002)

28. C. Li, C. Xu, C. Gui, and M. D. Fox. "Level set evolution without re-initialization: A new variational formulation." In *Proc. 2005 IEEE CVPR* (San Diego, 2005), pp. 1:430–436

29. L. Rudin, S. Osher, and E. Fatemi. "Nonlinear total variation based noise removal algorithms." Phys. D **60**, 259–268 (1992)

30. R. Kimmel. *Numerical geometry of images: Theory, algorithms, and applicaitions* (Springer, 2003)

31. K. N. Chaudhury and K. R. Ramakrishnan. "Stability and convergence of the level set method in computer vision." Pattern Recognition Lett. **28**, 884–893 (2007)

32. Y. Yu and J. A. Molloy. "Segmentation of the prostate from suprapubic ultrasound images." Med. Phys. **31**, 3474–3484 (2004)

33. Y. Yuan, M. L. Giger, K. Suzuki, H. Li, and A. R. Jamieson. "A two-stage method for lesion segmentation on digital mammograms." In *Medical Imaging: Image processing*, edited by J. M. Reinhardt and J. P. W. Pluim (2006), vol. 6144 of *Proc. SPIE*, pp. 61443W:1–5

34. S. A. Glantz. *Primer of biostatistics* (McGraw-Hill, New York, New York, 2002)

35. H. Li, M. L. Giger, Y. Yuan, L. Lan, K. Suzuki, A. R. Jamieson, and C. Sennett. "Comparison of computerized image analysis for digitized screen film mammograms and full field digital mammography images." In *Digital mammography*, edited by S. M. Astley, M. Brady, C. Rose, and R. Zwiggelaar (2006), vol. LNCS4046 of *IWDM 2006*, pp. 569–575

List of Figures

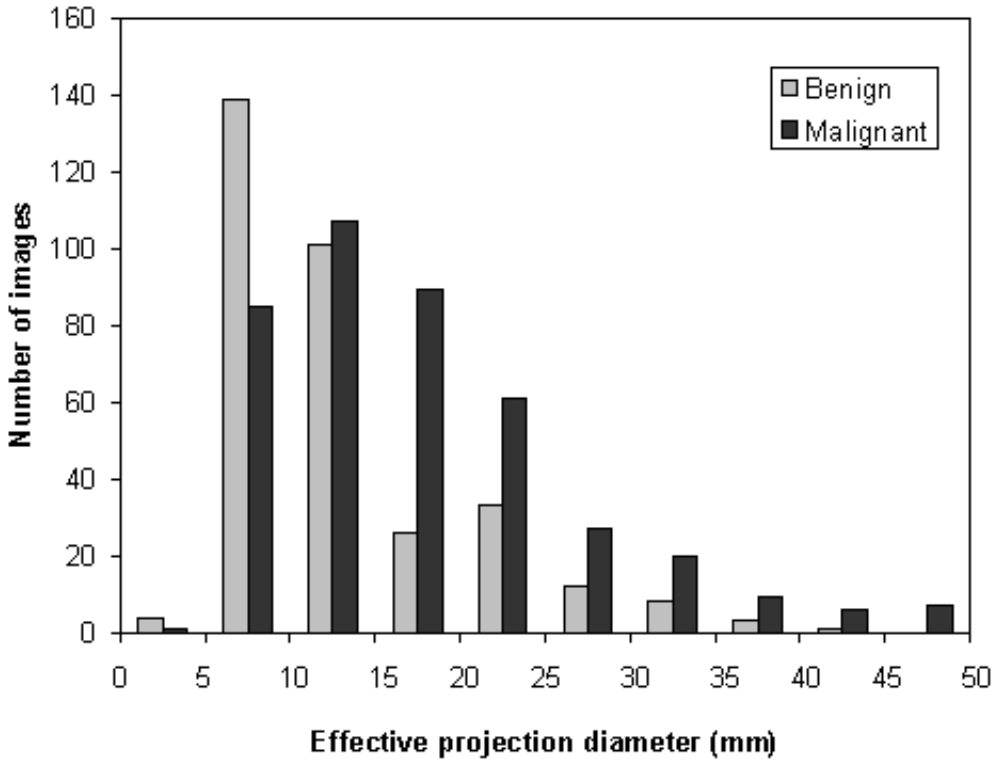

Figure 1: Distribution of lesions' effective diameters obtained from the FFDM database.

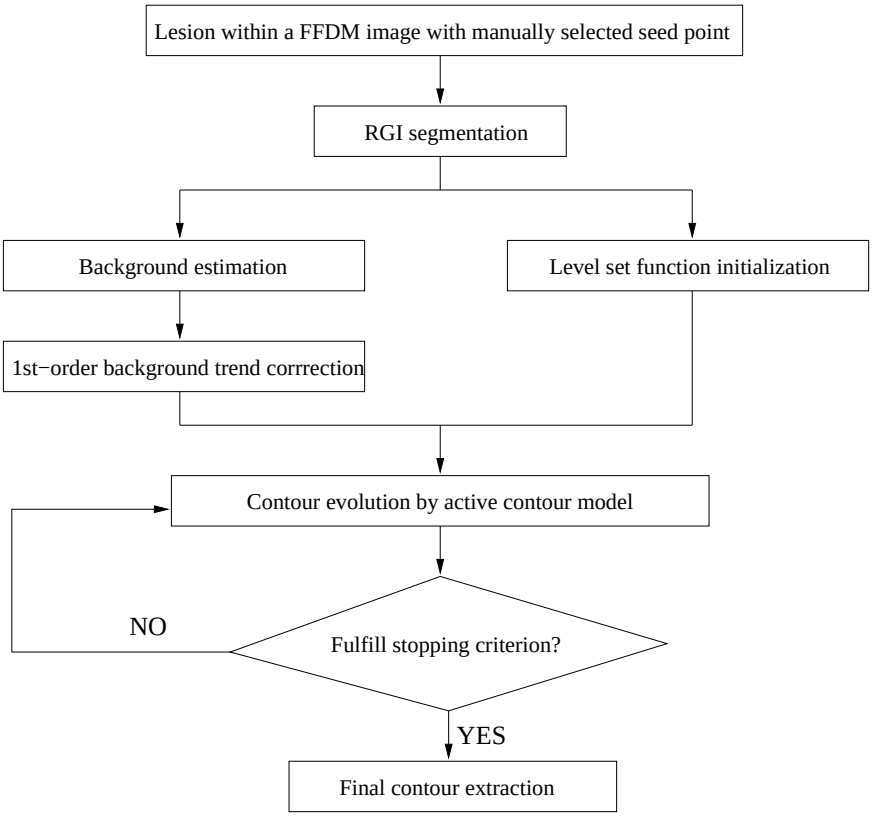

Figure 2: Schematic diagram of the proposed dual-stage lesion segmentation algorithm.

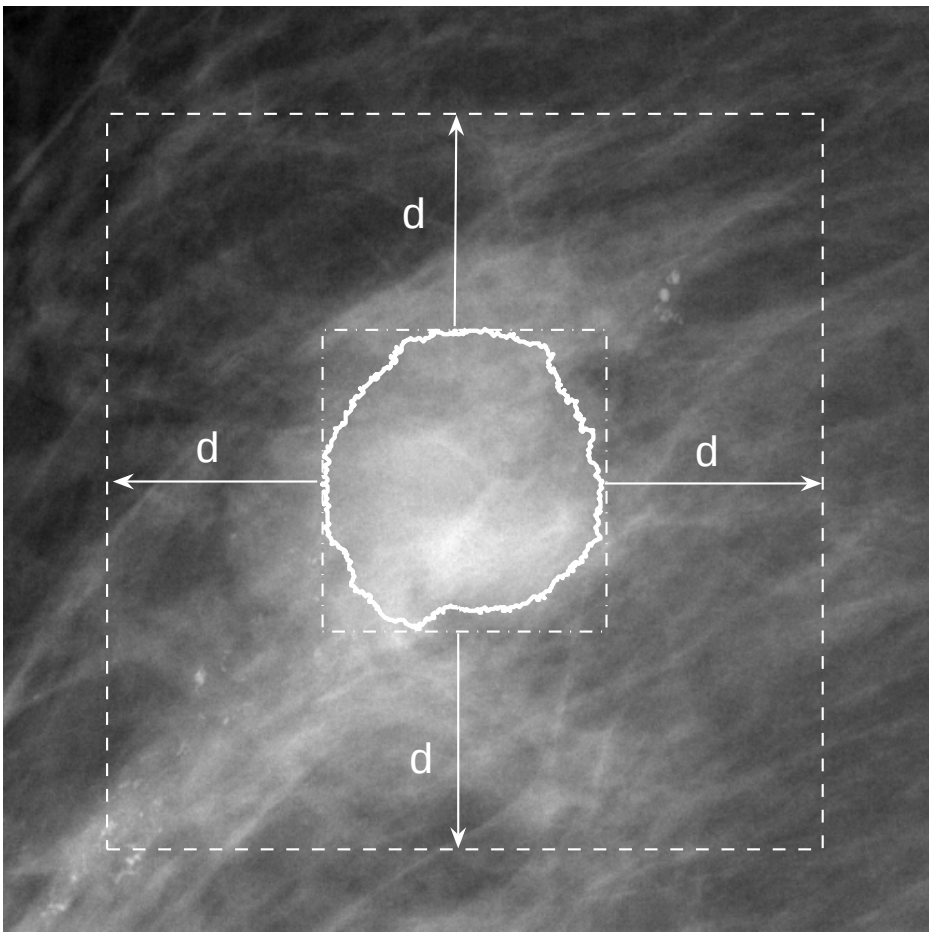

Figure 3: Illustration of defining the effective background. In this figure, the solid line represents the initial contour obtained by RGI segmentation and the dash-dotted rectangle is the circumscribed rectangle of this initial contour. The effective background is defined as the region inside the dashed rectangle excluding the region within the initial contour. An automatic scheme is employed to determine the best d.

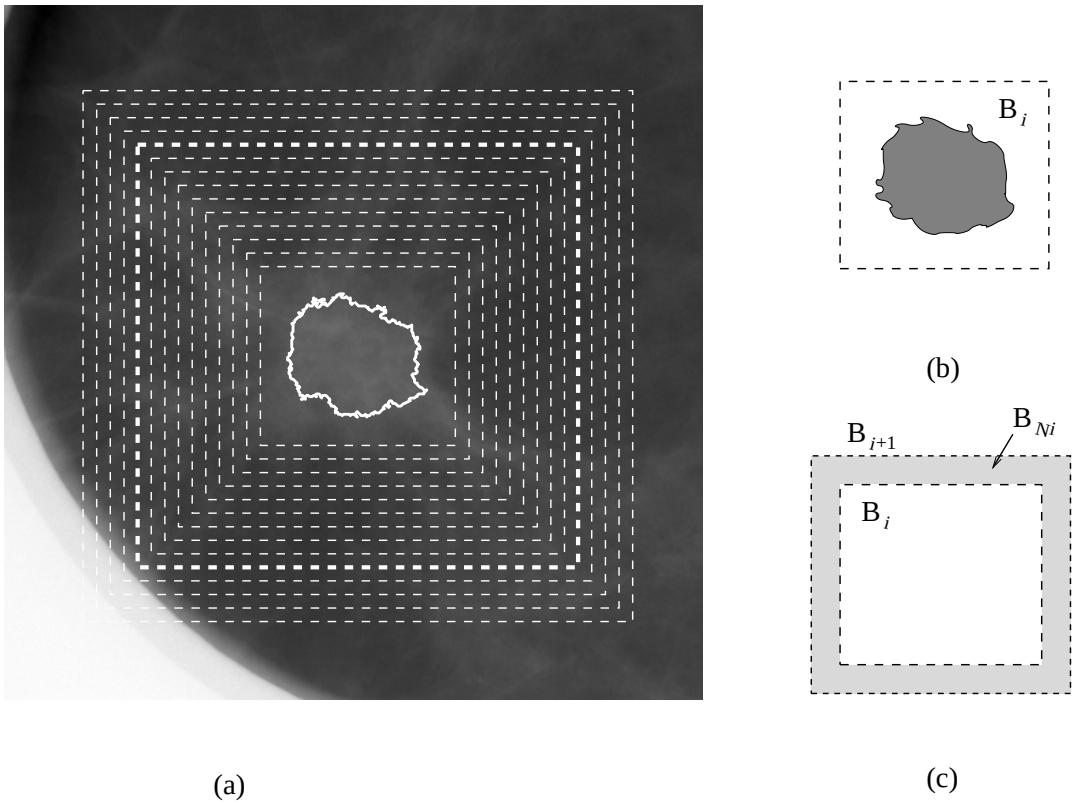

Figure 4: The illustration of determining the distance d. (a) a mammogram with a series of distances d_i, in which the thick dashed rectangle represents the computer-selected distance d ; (b) B_i: the ith background candidate corresponding to d_i ; (c) B_{Ni}: the ith net background increase. Background is defined as the set of pixels within a given distance d_i (pixel) from the circumscribed rectangle of the initial contour.

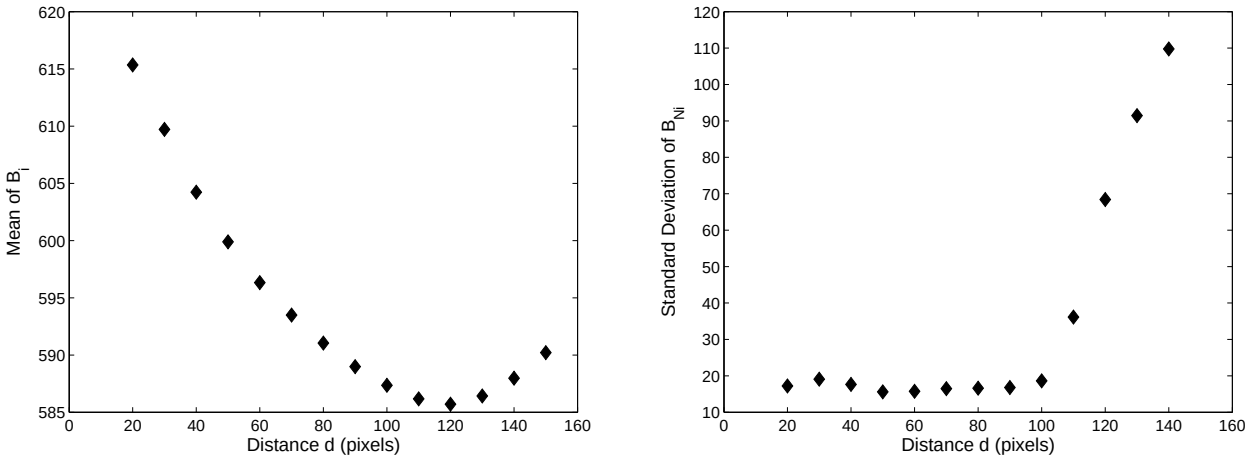

Figure 5: Left: the trend of mean value of B_i, the ith background candidate with respect to distance d_i. Right: the trend of standard deviation of B_{Ni}, the ith net background increase with respect to B_i and B_{i+1}.

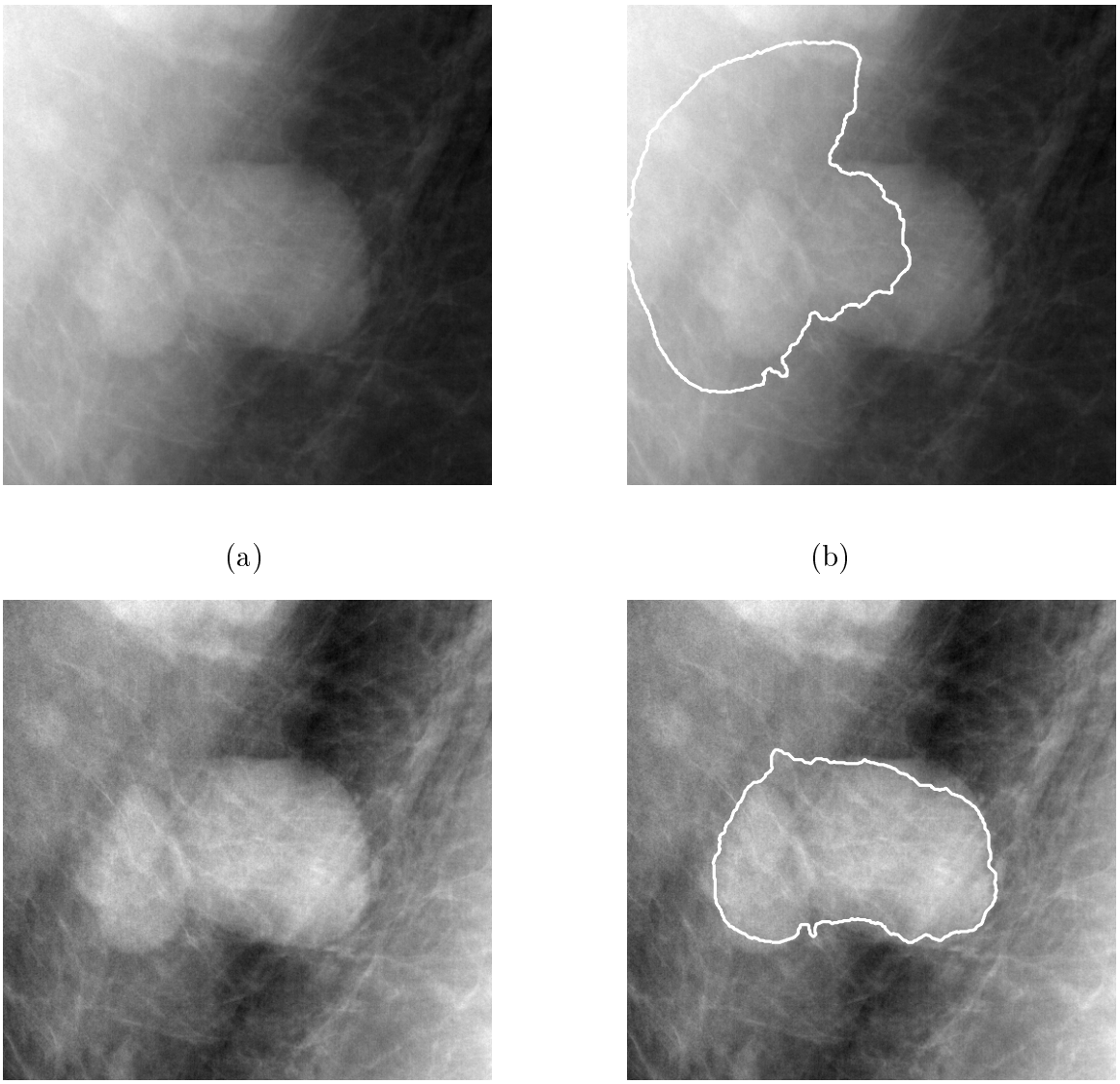

(a) (b)

(c) (d)

Figure 6: An example of the effect of background trend correction on segmentation. (a) the original ROI ; (b) segmentation result of (a); (c) the processed ROI after background trend correction; and (d) segmentation result of (c).

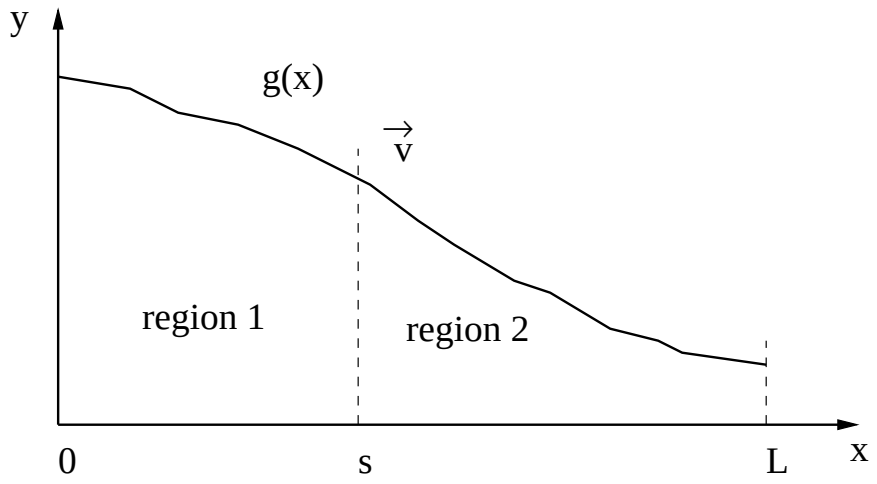

Figure 7: The illustration of determining the stopping point. $g(x)$ is a decreasing function defined on $[0,\ L]$ and $s \in [0,\ L]$ is a moving point with speed of $\vec{v}$.

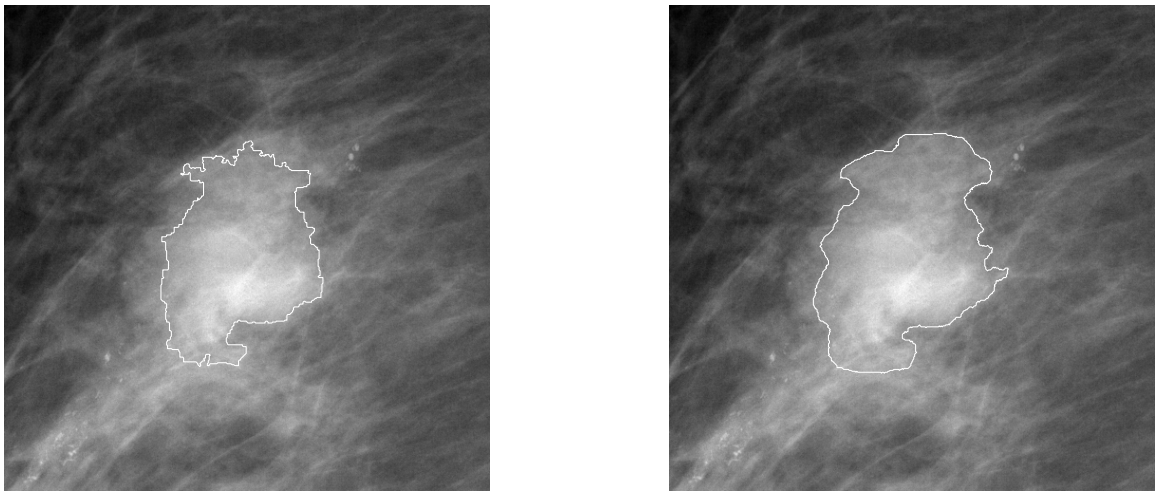

Figure 8: An example of the effect of level set smoothness to the final segmentation results. Left: segmentation without level set smoothness; Right: segmentation with level set smoothness.

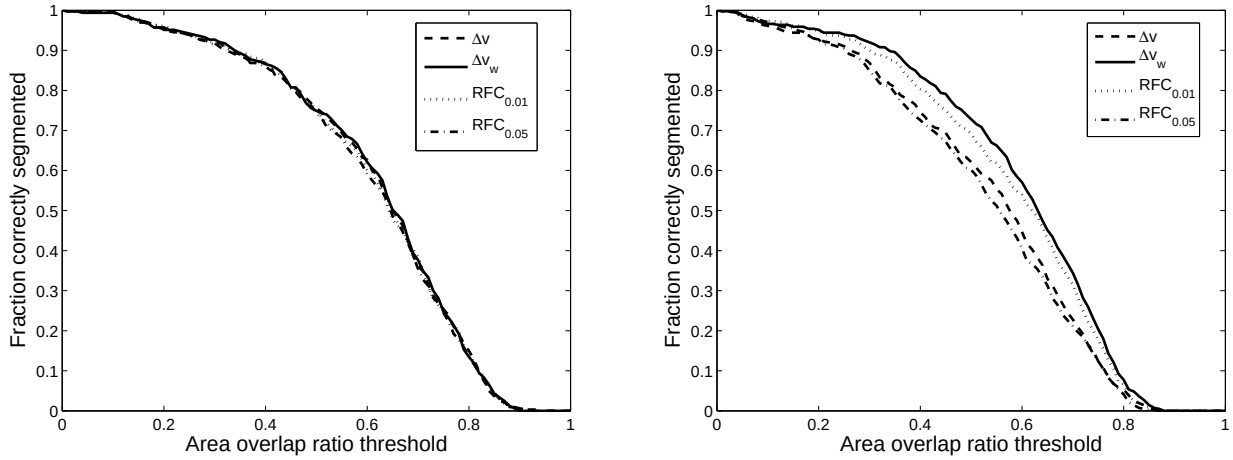

Figure 9: Segmentation performance of four different stopping criteria in terms of area overlap ratio (AOR) on a clinical FFDM database. In both plots, Δv_w is the weighted slope difference between foreground mean value and background mean value, in which foreground is the area within the evolving contour and background is the area outside contour; Δv is the unweighted slope difference between these two mean values. $RFC_{0.01}$ stands for a stopping criterion that terminates contour from evolution when the relative foreground change (RFC) is not greater than 0.01. Similarly, $RFC_{0.05}$ stops the contour evolution when RFC is not greater than 0.05. Left: evaluated on 327 benign images; Right: evaluated on 412 malignant images. The results show that the weighted slope difference is statistically superior to unweighted slope difference and convergence rate at $RFC = 0.05$ on malignant images.

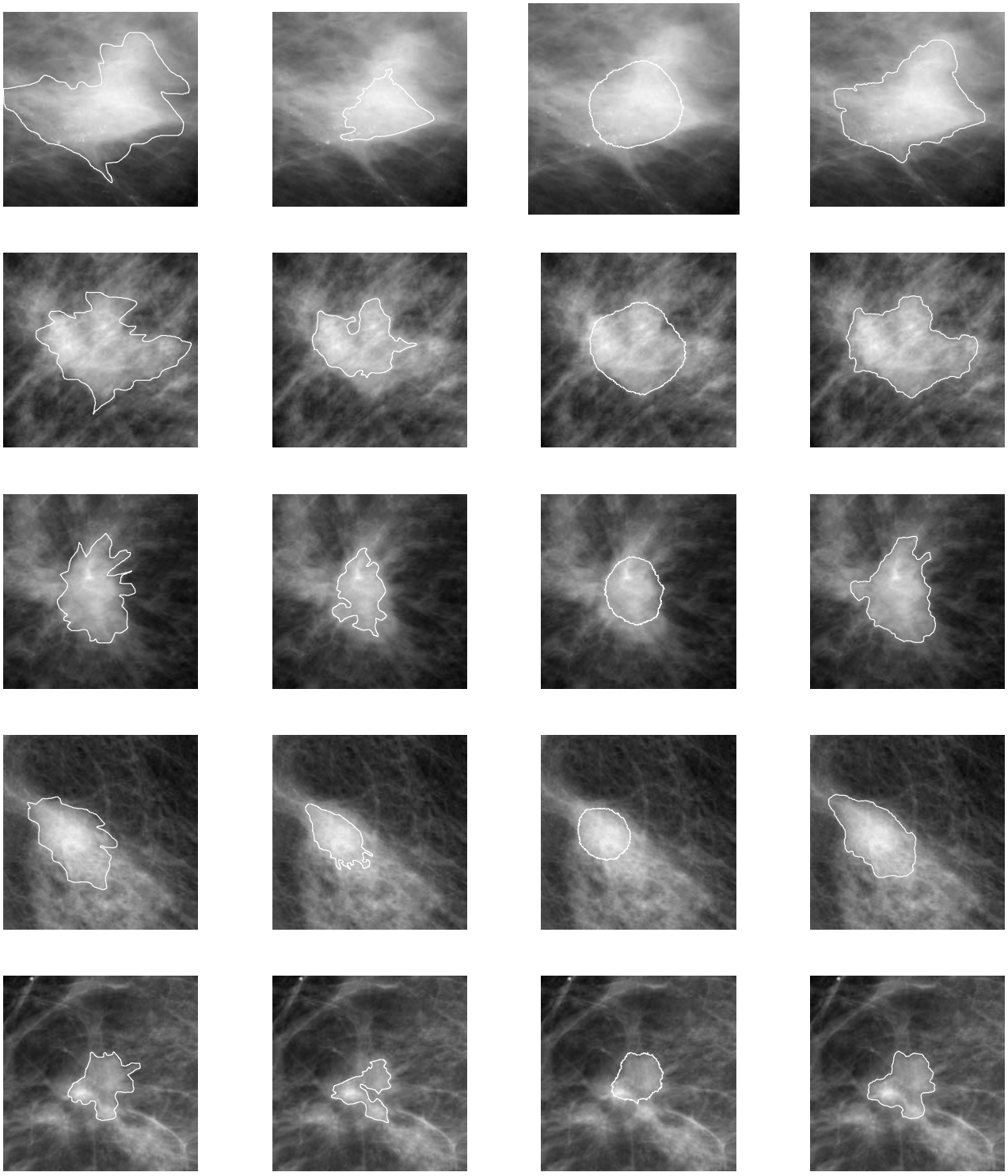

(a) (b) (c) (d)

Figure 10: Segmentation results for 5 malignant lesion examples. (a) radiologist's outline, (b) region-growing, (c) RGI-based segmentation and (d) the proposed dual-stage segmentation method

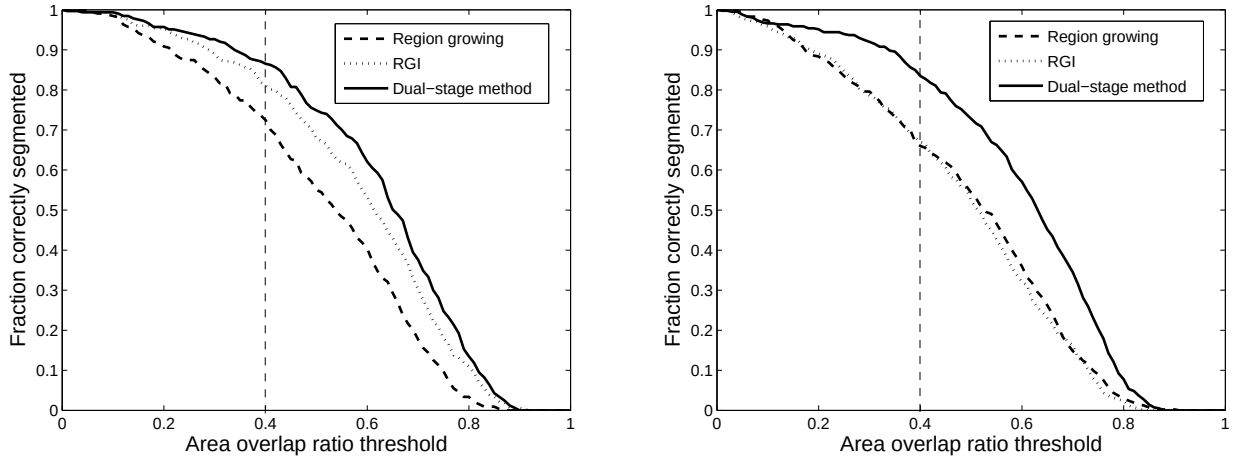

Figure 11: Performance of three different segmentation methods in terms of area overlap ratio (AOR) on a clinical FFDM database. Left: evaluated on 327 benign images; Right: evaluated on 412 malignant images. The results show that the dual-stage segmentation method is statistically superior to both region-growing and RGI-based method.

List of Tables

Table I: Statistical comparison of the performance of four stopping criteria in the dual-stage segmentation in terms of average area overlap (AOR), and p-values are given for the comparison of the weighted slope difference with any other stopping criterion. The significant level α_i for the individual paired t test is calculated using Holm's procedure (overall $\alpha^T = 0.05$). Same convention as Fig. 9.

		Δv_w	Δv	$RFC_{0.01}$	$RFC_{0.05}$
Benign					
	$mean \pm std$	0.61 ± 0.19	0.61 ± 0.19	0.61 ± 0.19	0.61 ± 0.19
	p-value	–	0.856	0.801	0.601
	sig. lev. (α_i)	–	–	–	–
Malignant					
	$mean \pm std$	0.59 ± 0.19	0.53 ± 0.20	0.57 ± 0.19	0.52 ± 0.20
	p-value	–	< 0.001	0.192	< 0.001
	sig. lev. (α_i)	–	0.05	–	0.025
All					
	$mean \pm std$	0.60 ± 0.19	0.57 ± 0.20	0.59 ± 0.19	0.56 ± 0.20
	p-value	–	0.002	0.25	< 0.001
	sig. lev.(α_i)	–	0.05	–	0.025

Table II: Statistical comparison of the three lesion segmentation algorithms. Performance is given by average area overlap ratio, and p-values are given for the comparison of the dual-stage segmentation with the previous region-growing and RGI-based method. The significant level α_i for the individual paired t test is calculated using Holm's procedure (overall $\alpha^T = 0.05$).

		Dual-stage segmentation	RGI	Region-growing
Benign				
	$mean \pm std$	0.61 ± 0.19	0.58 ± 0.19	0.51 ± 0.20
	p-value	–	0.01	< 0.001
	seg. lev. (α_i)	–	0.05	0.025
Malignant				
	$mean \pm std$	0.59 ± 0.19	0.48 ± 0.20	0.49 ± 0.20
	p-value	–	< 0.001	< 0.001
	seg. lev. (α_i)	–	0.025	0.05
All				
	$mean \pm std$	0.60 ± 0.19	0.52 ± 0.20	0.50 ± 0.20
	p-value	–	< 0.001	< 0.001
	seg. lev. (α_i)	–	0.05	0.025

TITLE:

Feature correlation on multiple-view FFDM images

AUTHORS:

Yading Yuan, Maryellen L. Giger, Hui Li and Charlene Sennett

PURPOSE: (473/2200)

The objective of this study is to evaluate the correlation performance of individual computerized features extracted from the full field digital mammograms (FFDM) of a lesion obtained in two different views. This research provides a guide for discriminating corresponding and non-corresponding lesion pairs within the CAD framework. It is also helpful for guiding the development of new features to improve the accuracy of image matching in disease diagnosis and prognosis.

METHOD AND MATERIALS: (1234/2200)

One dataset (A) includes 103 biopsy proven cases (48 benign solid lesions and 55 malignant lesions), each of which has a craniocaudal (CC) and mediolateral (ML) view. Another dataset (B) includes 52 cases (24 benign solid lesions and 28 malignant lesions), each of which has a CC and mediolateral oblique (MLO) view. In order to evaluate the robustness of the correlation performance to lesion segmentation, besides the radiologist's outlines, three automatic segmentation methods were employed to extract the mass lesion from the surrounding tissues. The conventional region-growing method uses abrupt changes in size and circularity as the rules of segmentation. The radial gradient index (RGI) based method applies RGI model to the suspicious lesion multiplied by a constraint function. The region-based active contour model evolves the contour based on the homogeneities both inside and outside of the evolving contour. Fifteen computer-extracted features of each lesion were calculated in both views in order to quantify the characteristics of margin, shape, contrast and texture of the lesion. For each feature, correlation coefficient between the two views and the p-value of the derived correlation coefficient were obtained.

RESULTS: (672/2200)

With the human outline, the feature characterizing the diameter of lesion yielded the correlation efficient of 0.87 for dataset A and 0.88 for dataset B, both of which have p-values far less than 0.05. The features characterizing shape, contrast and texture showed better performance among the 15 individual features despite of segmentation methods, pathology and the type of view pairs. This is because the features representing large-scale information are less sensitive to the change of position than those representing small-

scale information, which results in the higher correlation between large-scale features from different views than that of small-scale features.

CONCLUSIONS: (301/2200)

Our investigation indicates that the features that characterize the large-scale information of lesion have higher correlation between the two view images. We are currently applying these features to develop automated image matching method to determine corresponding and non-corresponding lesion pairs.

TITLE:

Correlative feature analysis of FFDM images

AUTHORS:

Yading Yuan, Maryellen L. Giger, Hui Li and Charlene Sennett

KEYWORDS:

Mammography, correlative feature analysis, computer-aided diagnosis

ABSTRACT:

Identifying the corresponding image pair of a lesion is an essential step for combining information from different views of the lesion to improve the diagnostic ability for both radiologists and CAD systems. Because of the non-rigidity of the breasts and the 2D projective property of mammograms, this task is not trivial. In this study, we present a computerized framework that differentiates the corresponding images from different views of a lesion from non-corresponding ones. A dual-stage segmentation method, which employs an initial radial gradient index (RGI) based segmentation and an active contour model, was firstly applied to extract mass lesions from the surrounding tissues. Then various lesion features were automatically extracted from each of the two views of each lesion to quantify the characteristics of margin, shape, size, texture and context of the lesion, as well as its distance to nipple. We employed a two-step method to select an effective subset of features, and combined it with a BANN to obtain a discriminant score, which yielded an estimate of the probability that the two images are of the same physical lesion. ROC analysis was used to evaluate the performance of the individual features and the selected feature subset in the task of distinguishing corresponding pairs from non-corresponding pairs. By using a FFDM database with 124 corresponding image pairs and 35 non-corresponding pairs, the distance feature yielded an AUC (area under the ROC curve) of 0.80 with leave-one-out evaluation, and the feature subset, which includes distance feature, lesion size and lesion contrast, yielded an AUC of 0.86.

DISCRIPTION OF PURPOSE:

Merging information from different views of a lesion has been widely recognized to allow radiologists to better detect and evaluate breast abnormalities in FFDM images. However, since a mammogram represents the 2D projection of the 3D distribution of attenuation coefficient, as well as the breast being a non-rigid object, the conventional image-registration techniques are not appropriate. In this study, we propose a computerized scheme, which relies on computer-extracted features instead of the original image, to determine if an image pair from different views represents the same lesion.

METHOD(S):

A dual-stage segmentation method was firstly applied to extract lesions from the surrounding tissues. This algorithm utilizes a geometric active contour model that maximizes an energy function based on the homogeneities inside and outside of the evolving contour. Prior to the application of the active contour model, a RGI-based method is applied to yield an initial contour close to the lesion boundary location in a computationally efficient manner.

Three groups of computer-extracted lesion features were used in our study. The first group includes features characterizing spiculation, margin, shape and contrast of a lesion, which are widely used for the task of distinguishing between malignant and benign lesions. The second group includes texture features extracted from various regions including the lesion, the surrounding neighborhood of the lesion, and the entire ROI, respectively. For each region, a 2D gray-level co-occurrence matrix (GLCM) was constructed, and texture features were extracted to quantify the spatial dependence of gray-level values. We developed an automatic

neighborhood estimation method to determine the effective circumstance of the lesion. The third group includes a distance feature calculated as the Euclidean distance from the nipple location to the center of the lesion. A nipple searching method was developed to identify the nipple location automatically.

A two-step method was employed for feature selection. A classifier was firstly applied to each single feature pair from different views, yielding a "correspondence" feature that represents the probability of corresponding pairs. Then, a linear stepwise feature selection method was used to select the effective subset of these correspondence features.

We used the BANN as our classifier, which incorporates Bayesian inference to avoid the problem of "over fitting". Receiver operating characteristic (ROC) analysis was used to assess the performance of the individual features and the selected feature subset in the task of distinguishing corresponding pairs from non-corresponding pairs.

RESULTS:

In our preliminary study, we tested the proposed scheme using a FFDM database, which includes 131 biopsy-proven lesions (63 benign and 68 malignant). From this database, we constructed 124 corresponding pairs and 35 non-corresponding pairs. Each pair consists of a craniocaudal (CC) view and a mediolateral (ML) view. Considering the most realistic scenario of lesion mismatch in clinical practice, the non-corresponding pairs were constructed from cases of the same patients but different physical lesions.

The correlation between the distance feature, from the automatic nipple identification method and those from manual nipple identification was 0.997 ($p<0.0005$). In leave-one-out evaluation by lesion, the distance feature outperformed among all the single features, yielding an AUC of 0.80. Distance feature, lesion size and lesion contrast were selected as the effective feature subset and yielded an AUC of 0.86. The improvement by using multiple features was statistically significant compared to single feature performance ($p = 0.0075$).

NEW OR BREAKTHROUGH WORK TO BE PRESENTED:

Our study includes three attractive features: 1) This correlative feature analysis (CFA) framework is based on computer-extracted features instead of original images, which is different from conventional image registration in which the registration is to align two images known to represent the same object, while the task of CFA is to evaluate the probability that the given two images represent the same object; 2) The newly developed distance feature improves the performance of single feature from AUC of 0.71 (lesion size) to 0.80 with leave-one-out evaluation ($p = 0.04$); 3) The first step of the new two-stage feature selection method effectively reduces the dimensionality of the feature space, and thus improves the performance to AUC of 0.86 with leave-one-out evaluation, as compared with 0.76 when applying the original features directly ($p=0.03$).

CONCLUSIONS:

We have presented a correlative feature analysis framework to estimate the probability that a given pair of two images as of the same physical lesion, and our investigation indicates that the proposed method is a promising way to distinguish between corresponding and non-corresponding pairs. We are collecting more cases to evaluate our method on a larger scale.

INDICATE WHETHER THE WORK IS BEING, OR HAS BEEN, SUBMITTED FOR PUBLICATION OR PRESENTATION ELSEWHERE, AND, IF SO, INDICATE HOW THE SUBMISSIONS DIFFER

No.